

Development of Multi-Fourier Transform interferometer :Fundamental

Izumi S. Ohta

National Astronomical Observatory 2-21-1 Osawa Mitaka Tokyo 181-8588, Japan¹

izumi.ohta@nao.ac.jp

Makoto Hattori

Tohoku University Aoba Aramaki Aoba-ku Miyagi 980-8488, Japan

Hiroshi Matsuo

National Astronomical Observatory 2-21-1 Osawa Mitaka Tokyo 181-8588, Japan

We propose the development of an instrument by the Martin & Puplett-type Fourier Transform Spectrometer to applying the aperture synthesis technique in millimeter and submillimeter waves. We call this equipment the Multi-Fourier Transform interferometer(MuFT). MuFT performs a wide band imaging, spectroscopy and polarimetry in millimeter and submillimeter wavelengths. We describe the fundamentals of MuFT, and give an example of one potential implementation. Full description of the observables by MuFT are provided. A physical explanation of the observability of the complex visibility by MuFT is given. Fundamental restrictions on observations with MuFT, eg. limits on spectral and spatial resolutions and field-of-view, are discussed. The advantages of MuFT are also summarized. © 2021 Optical Society of America

OCIS codes: 070.2590, 110.6770, 120.3180, 120.5410, 260.3090

1. Introduction

Astronomical observation of submillimeter waves represents one of the last unexplored regions of the electromagnetic spectrum. One of the difficulties with performing observations in this band is owing to a large atmospheric absorption. Since submillimeter waves are a boundary of the radio and infrared, there remain a lot of frontiers in the development of fundamental observational technology.

Radio interferometry and synthesis arrays, which are basically ensembles of two elements interferometers, are used to make measurements of fine angular resolution.¹ Interferometers have been

¹When this research was performed, Izumi S. Ohta was with Tohoku University Aoba Aramaki Aoba-ku Miyagi 980-8488, Japan. Izumi S. Ohta is now with National Astronomical Observatory 2-21-1 Osawa Mitaka Tokyo 181-8588, Japan

used at millimeter waves² and have been considered one of the best instruments at submillimeter wave.³ By setting two telescopes with separation larger than the maximum construct-able diameter of the single mirror, higher angular resolution than single dish system is easily achieved with aperture synthesis type interferometers. By combining many telescopes, a large effective area can be attained to increase the sensitivity of the system. Interferometers are robust against atmospheric fluctuations since large scale atmospheric fluctuations do not cause interference signals and are automatically omitted by the interferometers.

However, currently operating millimeter and submillimeter interferometers have the following two fundamental problems because they use heterodyne receivers as focal plane detectors: The receiving systems perform modulation and amplification of the source signal by mixing with a local oscillator signal. They can measure the phase of the incident electromagnetic wave. In the following discussion, the space-borne observation assumes as for an ideal case. The noise temperature of heterodyne receivers at frequency ν is written as $T_{sys-het} \sim 2(h\nu/k_B) \left[(\epsilon^2 n^2(\nu, T_0) + \epsilon n(\nu, T_0))^{\frac{1}{2}} + 1 \right]$, where n is the thermal Planck function with $T_0 = 2.73 K$ due to the cosmic microwavebackground (CMB), h and k_B are Planck constant and Boltzmann constant, respectively, and ϵ represents the detection efficiencies. The first term represents the photon noise due to statistical fluctuation of the CMB intensity. The second term represents the quantum limit of the heterodyne receivers which comes from the uncertainty principle between the phase and the number of photons.⁴ This equation shows that the noise temperature is limited by the quantum limit and is increased linearly with the frequency in the frequency range of $\nu > 100$ GHz. Therefore, the sensitivity of heterodyne-based interferometers is severely limited by the quantum limit of the receivers. Another problem is the severely limited field-of-view (FOV) of the interferometers, due to the difficulty of constructing a large format detector array of heterodyne receivers.⁴ In addition, the possible bandwidth of the interferometer is also limited by a bandwidth of Intermediate Frequency(IF) amplifier, since the phase change of the modulated signal after mixing with a local oscillator signal must be followed.

On the other hand, direct detectors such as bolometer are also used in millimeter and submillimeter systems except for interferometers. Direct detectors measure the intensity of the source signal. They cannot measure the phase of the incident electromagnetic wave. Therefore, they have not been used as focal plane detectors for interferometers. The quantum limit of a direct detector is the minimum detectable power when any internal noise can be neglected, the quantum limit of a direct detector is expressed in noise temperature as $T_{qu-dir} \sim h\nu/(k_B \Delta t \Delta \nu)$, where Δt and $\Delta \nu$ are the response time of the detector, which is about 1 – 100 msec in the case of bolometer, and the bandwidth of the detector, which is about 10 – 100 GHz.⁴ The noise temperature of direct detectors at frequency ν is written as $T_{sys-dir} \sim 2(h\nu/k_B) \left[(\epsilon^2 n^2(\nu, T_0) + \epsilon n(\nu, T_0))^{\frac{1}{2}} + 1/\Delta t \Delta \nu \right]$. The second term is negligible compared with the CMB photon noise at millimeter and submillimeter waves. Therefore, noise temperature of direct detectors are much lower than heterodyne receivers in the frequency range of $\nu > 100$ GHz. Actually, the noise power of the most sensitive currently operating bolometers is already lower than the quantum limit of the heterodyne in the frequency range of $\nu > 100$ GHz. In Contrast to the heterodyne, a large format millimeter and submillimeter direct detector array is possible to construct.^{5,6} There is essentially no limit on the

bandwidth for direct detectors.⁷

The above discussion indicates that the bolometric interferometer, which is able to use a direct detector as a focal plane detector for the interferometer, could be one of the best ideal instruments for millimeter and submillimeter astronomy since it shares the advantages of both direct detectors and interferometer. Since direct detectors cannot obtain the information of the phase of electromagnetic waves, two beams captured by two apertures must be mixed before guided into the detectors. There are two ways to mix beams. One is called Fizeau type beam mixing. The simplest example of this method is that two beams obtained by masking a single telescope are mixed at the focus of the telescope. Images of different portions of the sky are focused on different positions of the focal plane. Therefore, the extension of the FOV by using the focal plane detector array is straightforward in this case. However, there is a fundamental problem in applying this method to millimeter and submillimeter observations. We have to use many detector pixels within a single FOV to resolve the fringe pattern inside of the FOV. Since the direct detector arrays in millimeter and submillimeter wave bands are still expensive, the cost performance of applying this method to this waveband is poor. The other method is called the Michelson-type beam mixing. An application of the Fourier Transform Spectrometer (FTS) to aperture synthesis interferometry has been studied as a possible solution of the Michelson-type beam mixing bolometric interferometer. The application was first independently proposed by Itoh & Ohtsuka(1986)⁸ and Mariotti & Ridway (1988)⁹ in near infrared (NIR). The system was referred by these authors as "double Fourier interferometry", since the signal obtained by the system is a Fourier transformation of both spectra and intensity distribution on the sky. Itoh & Ohtsuka studied single pupil interferometry. Mariotti & Ridway studied multi-pupil interferometry for high spatial resolution. As explained in this paper, the extension of the FOV by putting the focal plane detector array is not straightforward, but it is possible with some restrictions. Rinehart et al. (2004)¹⁰ have been studying the extension of the FOV by putting a detector array on the focal plane of the double Fourier in laboratory experiments in an optical wave bands by using optical CCD camera. They refer to this experiment as the Wide-field Imaging Interferometry Testbed.

In this paper, we propose the application of a Martin & Puplett-type Fourier Transform spectrometer (Martin & Puplett(1969),¹¹ hereafter MP-FT) to the aperture synthesis system in millimeter and submillimeter waves(Ohta(2004)¹²). A wire grid polarizer (WG) is used as a beam splitter in this system. So, the wavelength dependence of reflectivity of WG is small and is suitable for a wide band measurement system. By setting the two input WGs appropriately, 2D intensity distribution of four Stokes parameters can be measured. The signal obtained by our system is a Fourier transformation of spectra and intensity distributions of four Stokes parameters (multiple components) on the sky. Therefore, we refer to this system as a Multi-Fourier Transform interferometer, abbreviated to MuFT. The abbreviation also contains the meaning that this instrument measures Mutual correlation of the source signal instead of auto-correlation as in the case of usual FTS.

The plan of this paper is as follows: In Section 2, fundamentals of imaging and spectroscopy by MuFT are explained using scalar waves for simplicity. How complex visibility is measured by MuFT is also explained in Sec. 2. In Sec. 3, details of the components of MuFT are introduced. A full

description of the observables by the MuFT and restrictions intrinsic to MuFT are also provided in Sec. 3. In Sec. 4, the advantages of the MuFT are summarized. A summary of the paper is given in Sec. 5. This paper presents the fundamental theory of MuFT. Details of broadband imaging and spectroscopy experiments using MuFT are presented in a forthcoming paper.

2. Fundamentals of Multi-Fourier Transform interferometer

2.A. Fundamentals of imaging by MuFT

Coordinate systems on the source plane and the observer plane are defined in Fig. 1. The notation of this coordinate system follows Born & Wolf.¹³ The coordinate system on the source plane (ξ, η) is fixed on the sky. The origin of the coordinate system on the source plane is defined to the center of the FOV. The coordinate system on the observer plane is defined as X and Y axes that are parallel to ξ and η axes, respectively. The origin of the observer coordinate is defined as the mid-point of two apertures mounted at P_1 and P_2 . The position vector connecting to the center of the aperture mounted at P_2 with the center of the aperture mounted at P_1 is defined as $\mathbf{b} = (b_x, b_y)$, which is referred to as the baseline vector. No absorption, no emission and no scattering due to matter distributed between the source and observer are assumed.

We consider the measurement of the mutual coherence function of the waves obtained by two apertures P_1 and P_2 . The source electric fields arrived at P_1 and P_2 are defined as $E_{P_1}(t)$ and $E_{P_2}(t)$, respectively. They are recombined at Q. When two beams are recombined at Q, there is a time lag τ which is caused by the internal light path length difference from each aperture to Q, that is $\tau = (\ell_1 - \ell_2)/c = 2x/c$. The mutual coherence function with the time lag τ is defined as

$$\Gamma_{12}(\tau) \equiv \langle E_{P_1}(t)E_{P_2}^*(t + \tau) \rangle, \quad (1)$$

where $\langle \rangle$ denotes time average. The intensity of the recombined signal is written as

$$I_{12}(Q, \tau) = I_1 + I_2 + 2\Gamma_{12}^{(r)}(\tau), \quad (2)$$

where I_1 and I_2 are the intensities of the signals obtained by each aperture and $\Gamma_{12}^{(r)}(\tau)$ is a real part of $\Gamma_{12}(\tau)$. The unwanted DC components could be subtracted, and are neglected in the following discussion. Since the sizes of the astronomical objects are much larger than the wavelengths of the electromagnetic waves which we are interested in, any astronomical extended source can be treated as a collection of incoherent point sources except for a few exceptional cases. A viewer angle of the source from the observer plane is introduced as $\boldsymbol{\theta} = (\theta_x, \theta_y) = (\xi/R, \eta/R)$. Then, the mutual coherence function and its real part can be expressed by the specific source intensity, $I(\boldsymbol{\theta}, \nu)$, as

$$\Gamma_{12}(\mathbf{b}, \tau) \equiv \Gamma_{12}(\tau) = \int_{\Omega} \left\{ \int I(\boldsymbol{\theta}, \nu) \exp \left[-2\pi j \frac{\nu}{c} (\mathbf{b} \cdot \boldsymbol{\theta}) + 2\pi j \nu \tau \right] d\nu \right\} d^2\boldsymbol{\theta}, \quad (3)$$

$$\Gamma_{12}^{(r)}(\mathbf{b}, \tau) \equiv \Gamma_{12}^{(r)}(\tau) = \int_{\Omega} \left\{ \int I(\boldsymbol{\theta}, \nu) \cos \left[-2\pi \frac{\nu}{c} (\mathbf{b} \cdot \boldsymbol{\theta}) + 2\pi \nu \tau \right] d\nu \right\} d^2\boldsymbol{\theta}, \quad (4)$$

where Ω is the solid angle expanded by the source, j is an imaginary unit, and $\Gamma_{12}(\mathbf{b}, \tau)$ and $\Gamma_{12}^{(r)}(\mathbf{b}, \tau)$ explicitly express the dependence of the mutual coherence function on the baseline vector. The intensity expressed in Eq. (4) is the observable by MuFT.

The spectroscopy-resolved source image is extracted from the observed $\Gamma_{12}^{(r)}$ in the following way: For each fixed combination of \mathbf{b} , $\Gamma_{12}^{(r)}$ is measured for the time lag from $-\tau_0$ to τ_0 by changing ℓ_2 continuously. By performing a Fourier integration of the obtained $\Gamma_{12}^{(r)}$ in τ , the spectrally resolved mutual coherence function, $\hat{\Gamma}_{12}(\mathbf{b}, \nu)$, is obtained as

$$\hat{\Gamma}_{12}(\mathbf{b}, \nu) = \int_{\Omega} \left\{ \int I(\boldsymbol{\theta}, \nu') 2\tau_0 \text{sinc}[2\pi(\nu' - \nu)\tau_0] \exp\left[-2\pi j \frac{\nu'}{c} (\mathbf{b} \cdot \boldsymbol{\theta})\right] d\nu' \right\} d^2\boldsymbol{\theta}, \quad (5)$$

where $I(\boldsymbol{\theta}, -\nu) = I(\boldsymbol{\theta}, \nu)$ is used and $\text{sinc } x = (\sin x)/x$. This is a kind of Winner-Khynchine Formula.¹³ The integration by ν' reduces to $\nu' = \nu$ with spectral resolution of $\Delta\nu \sim 1/\tau_0$. Since $\nu \gg 1/\tau_0$ in an usual case, $\Delta\nu \ll \nu$. Now the customary notations in the interferometer can be introduced, that is

$$u = \frac{b_x \nu}{c} = \frac{b_x}{\lambda}, \quad v = \frac{b_y \nu}{c} = \frac{b_y}{\lambda}. \quad (6)$$

The (u, v) is called spatial frequency. When $|\mathbf{b} \cdot \boldsymbol{\theta}| \Delta\nu/c \ll 1$, the Fourier transformation of the mutual coherence function can be written as

$$\hat{\Gamma}_{12}(u, v, \nu) = \int_{\Omega} \tilde{I}(\boldsymbol{\theta}, \nu) \exp[-2\pi j(u\theta_x + v\theta_y)] d^2\boldsymbol{\theta}, \quad (7)$$

where \tilde{I} is a spectrally convolved source intensity distribution defined as

$$\tilde{I}(\boldsymbol{\theta}, \nu) = \int I(\boldsymbol{\theta}, \nu') 2\tau_0 \text{sinc}[2\pi(\nu' - \nu)\tau_0] d\nu'. \quad (8)$$

The functional form of the convolution kernel depends on the apodization function adopted when the Fourier transformation by τ is performed. In the above example, the top hat function is adopted as the apodization function. Eq. (7) is equivalent to the equation which expresses the van Cittert-Zernike Formula in Fraunhofer limit.¹³ It shows that the Fourier transformation of the mutual coherence function, $\hat{\Gamma}_{12}(u, v, \nu)$, is the complex visibility function of the source except for the proportionality constant. The main reason why the MuFT is capable of measuring the source complex visibility function, is to take data about the time lag τ from $-\tau_0$ to τ_0 symmetrically. By Fourier transforming them in u and v , source images are obtained for various frequencies. The MuFT is, in principle, is capable of performing simultaneous measurements of source image and spectrum. The MuFT corresponds to the XF-type radio interferometer.¹ Physical explanation of the principles of imaging by MuFT is given in Sec.2B.

The observability of the complex visibility function by MuFT makes observations with MuFT easier. From Eq. (7) $\hat{\Gamma}_{12}^*(u, v, \nu) = \hat{\Gamma}_{12}(-u, -v, \nu)$. Here we have used the fact that the source intensity distributions, $I(\boldsymbol{\theta}, \nu)$, are a real variable called the reality condition. Therefore, sampling in only half of the uv plane is enough to perform imaging observations by MuFT.

Large dynamic range advantage When the source intensity distribution does not depend on frequency, all the source images obtained for various frequencies can be summed up into a single image in the following way: In this case, the frequency dependence $i(\nu)$ and the spatial coordinate dependence of the source intensity $B(\boldsymbol{\theta})$ are decomposable, such as $I(\boldsymbol{\theta}, \nu) = B(\boldsymbol{\theta})i(\nu)$.

The spectrally convolved source intensity distribution can also be written as $\tilde{I}(\boldsymbol{\theta}, \nu) = B(\boldsymbol{\theta})\tilde{i}(\nu)$ where $\tilde{i}(\nu)$ is the convolution of $i(\nu)$ with the spectral convolution kernel. Eq. (7) can be rewritten as

$$\hat{\Gamma}_{12}(u, v, \nu) = \int_{\Omega} B(\boldsymbol{\theta}) \tilde{i}(\nu) \exp \left[-2\pi j \frac{\nu}{c} (\mathbf{b} \cdot \boldsymbol{\theta}) \right] d^2\theta. \quad (9)$$

Divided by $\tilde{i}(\nu)$, the frequency dependence of the source intensity can be removed.

Suppose that the observations for the baseline vector combinations on a circle with a radius of $|\mathbf{b}| = b$ on the baseline vector plane were performed with continuous sampling. Observed frequency bandwidth is supposed to be very wide. Adopt a polar coordinate on the baseline vector plane as $\mathbf{b} = (b, \varphi)$. Integrate $\hat{\Gamma}_{12}(\mathbf{b}, \nu) \exp[2\pi j \nu (\mathbf{b} \cdot \boldsymbol{\theta})/c] / \tilde{i}(\nu)$ by $\nu d\nu$ and $(b^2/c^2)d\varphi$ for a fixed b . Transform variables from ν and φ to $u = b\nu \cos \varphi/c$, $v = b\nu \sin \varphi/c$ using $\partial(u, v)/\partial(\nu, \varphi) = \nu b^2/c^2$. This procedure leads to the source intensity distribution as

$$\begin{aligned} & \int_0^{2\pi} \left\{ \int_0^{\infty} \nu \frac{\hat{\Gamma}_{12}(\mathbf{b}, \nu)}{\tilde{i}(\nu)} \exp \left[2\pi j \frac{\nu}{c} (\mathbf{b} \cdot \boldsymbol{\theta}) \right] d\nu \right\} \frac{b^2}{c^2} d\varphi \\ &= \int_0^{2\pi} \left\{ \int_0^{\infty} \nu \int_{\Omega} d^2\theta' B(\boldsymbol{\theta}') \exp \left[-2\pi j \frac{\nu}{c} (\mathbf{b} \cdot \boldsymbol{\theta}') \right] \exp \left[2\pi j \frac{\nu}{c} (\mathbf{b} \cdot \boldsymbol{\theta}) \right] d\nu \right\} \frac{b^2}{c^2} d\varphi, \\ &= \int_{-\infty}^{\infty} \left(\int_{\Omega} B(\boldsymbol{\theta}') \exp \left\{ 2\pi j \left[u(\theta'_x - \theta_x) + v(\theta'_y - \theta_y) \right] \right\} d^2\theta' \right) dudv, \\ &= \int_{\Omega} B(\boldsymbol{\theta}') \delta^2(\boldsymbol{\theta}' - \boldsymbol{\theta}) d^2\theta', \\ &= B(\boldsymbol{\theta}). \end{aligned} \quad (10)$$

In essence, the procedure can be thought of as follows: Since the spatial distribution is independent of frequency, the choice of frequency to measure the source intensity distribution is arbitrary. For a fixed baseline interval, observations with short wavelengths measure precise structures with high resolution and observations with long wavelengths measure overall structures with low resolution. By gathering all this information, precise source intensity distribution is obtained.

Several modifications are required to apply the above procedure to real observations. First of all, sampling on the baseline vector plane can neither be perfect nor continuous. The sampled points on this plane will be discrete and sparse. Instead of the Fourier integration described in Eq. (10), discrete Fourier transformation must be performed. To express the sparseness of the sampled points, convolution with a window function which is set at zero at the baseline vector points where the observation was not performed, must be taken into account in this calculation. Secondly, the source spectrum may not be finite for all frequencies. The source intensity may be zero in some frequency ranges due to absorption by the intervening medium or no emission from the source. Division by $\tilde{i}(\nu)$ described in Eq. (10) will diverge in these frequency ranges. The data for these frequency ranges should be removed in the procedure. Otherwise, they may introduce a large amount of noise into the obtained map. These modifications result in an imperfect map. However, it does not mean that the intrinsic power of the large dynamic range advantage is lost. The imperfection of the synthesized map due to the imperfect uv coverage is one of the most common problems in interferometer. The

large dynamic range advantage of MuFT can be explained as a large uv coverage being obtained from a small number of baseline vector combinations. This technique is essentially the same as the Multi-Frequency Synthesis (MFS) used in radio interferometers (Conway et al.(1990)¹⁴).

The situation to which this procedure is applicable is a very special case. However, there are plenty of astronomically important objects whose spatial distribution is independent on frequency, such as millimeter and submillimeter wave intensity distribution of clusters of galaxies known as Sunyaev-Zel'dovich effect (hereafter SZ effect, Sunyaev & Zel'dovich (1972),¹⁵ Hattori & Okabe(2005)¹⁶).

2.B. The physical explanation of imaging by MuFT

As shown in the previous section, the essential reason why MuFT is capable of performing imaging observations in broadband is that the complex visibility function of the source can be extracted from the observables with MuFT. This is accomplished by changing the time lag from $-\tau_0$ to τ_0 symmetrically. The reason why the complex visibility function is measurable by this process, is physically explained as follows.

Consider a broadband point source observation by MuFT. Suppose that there is a geometrical time lag, τ_g , caused by the light path length difference from the source to each aperture P_1 and P_2 , that is $\tau_g \equiv (R_1 - R_2)/c$. A burst-like interference signal is observed as scanning in τ by changing ℓ_2 continuously at $\tau = -\tau_g$, where the geometrical time lag is compensated by the internal time lag. Since this burst-like signal always appears at $\tau = 0$ in the FTS, the signal appearing at $\tau = 0$ is called a central burst of the interferogram. We also refer to this burst-like signal observed for a point source in MuFT to a central burst as following the FTS. In the case of MuFT, the burst center appears at the position where the total time lag of the light led by each aperture is zero. The position of the central burst observed by MuFT contains information about the position of the point source in the sky. If the source position is slightly shifted from the origin of the source plane toward the same side of the aperture P_1 and τ_g is negative, then τ must be positive and vice versa to observe the central burst signature. Suppose that τ is only scanned in the positive range. The central burst of the second source is not observable by this scan and we cannot know the position of the second source. By rotating the baseline vector by 180 degrees if possible, the geometrical time lag for the second source becomes negative and the central burst caused by the second source becomes observable by the positive τ scan. On the other hand, the central burst of the first source goes out of the positive τ region. This rotation corresponds to take a $-\mathbf{b}$ configuration of two apertures. Therefore, when τ is scanned only in the positive range, to obtain a full source image, measurements with \mathbf{b} and $-\mathbf{b}$ configurations are required. However, if we allow for scanning of the negative τ region, the central burst of the second source can be detected in the negative τ region without rotating the baseline vector. Therefore, by performing a scan in τ from the negative to the positive range symmetrically, the full source image is measurable without a performing 180-degree rotation of the baseline vector. This is why the symmetrical scan in τ leads us to obtain the complex visibility function.

In contrast to the MuFT, the complex visibility function is obtained in the following ways in the heterodyne system: The real part of the complex visibility function is obtained by directly

correlating the signals obtained by each aperture. The imaginary part is obtained by correlating the signals after applying the $\pi/2$ phase shifter for one of the signals.

3. The application of the Martin & Puplett-type FTS to aperture synthesis

3.A. Components of MuFT

Fig.2 is a schematic diagram of the MuFT system. From the top of the page, the parts depicted are the Light Collecting unit(LiC), the Fourier Interference unit(FI) and the Detection & Sampling unit(DeS). The detected signal is transferred to a computer after it has been through an electrical amplifier, a noise filter and an AD converter. The sampled data are analyzed by a data analysis system. Since the data is transformed into Polarimetry, Spectroscopy and Imaging information in the data analysis system, the data analysis system is referred to as PSI.

The LiC first part performs a division of the wave front of the incident source signal, and guides the signal to the Fourier Interference unit. Two different types are considered. One type has multi-apertures installed on separated multi-platforms. The antenna in multi-platforms type radio interferometer and siderostat in multi-platforms type optical-IR interferometer correspond to this type. In this type, there are large geometrical time lags except for the moment when the source is at southing. To compensate for the geometrical time lags which are also time-variable due to earth rotation, a large and time-variable offset in the scanning center of τ must be introduced in MuFT. To do this, a fringe tracking delay-line technique can be applied.¹⁷ When the MuFT system is applied to multi-platforms type LiC, performing a symmetrical scan in τ from the negative to the positive region is essential to obtain the complex visibility function. This is because the possible rotation angle of the baseline vector relative to the astronomical sources is limited, since the sources set and are not observable for nearly half a day except for sources around a celestial pole. The other type of LiC has that multi-apertures are installed on a single platform. For simplicity, we consider the two-aperture case. The positions of the two telescopes are controlled by controlling the azimuth and elevation angles of the platform so that a fixed reference point on the targeted source is maintained by a baseline vector bisector line, perpendicular to the baseline vector. The same reference point must be kept in the center of the FOV of each telescope. Examples of this type of LiC are CBI¹⁸ and AMiBA¹⁹ which have multi apertures installed on a single platform. Two mirrors connected by one rail mounted on a turntable, such as SPIRIT (Mather & Leisawitz(2000)²⁰), could be a solution. In the space, using multi-satellites could be an attractive solution.

The Fourier Interference unit is an instrument in which divided light beams are recombined after modulating one of the light path lengths to make an internal time lag and is the heart of the MuFT system. The method of beam mixing is the Michelson type, as mentioned in the introduction. This is designed by applying the MP-FT to aperture synthesis. It has two entrance windows to receive two light beams guided from the light collecting unit. Wire grid polarizers are used as beam splitters and beam combiners. One example of the FI unit is shown in Fig.3.

The direction of the WGs 1 and 2 wires must be set in the following ways. Consider light rays which enter the WGs 1 and 2 along the vertical axis. These rays are reflected by the WGs and travel

toward the Roof Top Mirrors (RTM) along a horizontal axis, and are then reflected by RTMs and travel back toward the WGs 1 and 2. Consider the projection of the WGs 1 and 2 on the planes normal to these light rays. The wires of these WGs must be tilted 45 degrees from the vertical axis on these planes. There are two possibilities for the wires being tilted clockwise (CW) or counter clockwise (CCW) from the vertical axis. There are four combinations for the alignment of the WGs 1 and 2. Two basic configurations of the WGs are illustrated in Fig.4. When the wires of both WGs are set in a CW direction, Stokes parameters of \mathcal{I} and \mathcal{Q} are observable. This is referred to as option 1. By setting both WGs to CCW, complementary data for the first case is obtained. One of the configurations gives $\mathcal{I} + \mathcal{Q}$ and the other gives $\mathcal{I} - \mathcal{Q}$. When the wires of WG 1 are set CW and those of WG 2 are set CCW direction, Stokes parameters of \mathcal{U} and \mathcal{V} are observable. This is referred to as option 2. By changing the setting of WGs 1 and 2 vice versa, complementary data for the original combination are obtained. One of the configurations gives $\mathcal{U} + \mathcal{V}$ and the other gives $\mathcal{U} - \mathcal{V}$. Therefore, by performing observations with all four combinations, spectrally resolved source intensity distributions of 4 Stokes parameters are obtained. Since only three of 4 Stokes parameters are independent for completely polarized waves, systematic errors could be self calibrated in MuFT by measuring all 4 Stokes parameters for the completely polarized light beams. For the intensity measurement, observations with option 1 is enough. Details are explained in the next subsection.

The other WGs installed in the FI unit for each option must be aligned in the following ways: In option 1, the wires of BS WG must be directed vertically or horizontally as illustrated in Fig.3 to combine the two beams taken by WGs 1 and 2 at BS. The combined beam, either reflected or transmitted by BS, is led to WGs A or B. To get interference terms of the two beams, the wires of output WGs A and B must be tilted 45 degrees from the vertical axis on the projected plane normal to the transmission axis. In option 2, the wires of BS WG projected on the same plane as the projection plane for WG 2 must be perpendicular to those of WG 2. Then, the beam taken by WG 1 is transmitted and the beam taken by WG 2 is reflected by BS WG, and those are led to output WG A. The wire of output WG A must be vertical or horizontal to get interference terms of the two beams.

To extract the maximum ability of MuFT, direct detectors like a bolometer, which performs broadband intensity measurement, must be mounted on the DeS unit. One of two bolometers detects transmitted signals through the output WG, while the other detects reflected signals. The difference in reflected and transmitted signals reproduces the full mutual coherence function since the phase difference in the interferograms between two signals is π . Also, unwanted DC components are removed by this process. The DC fluctuations originating in the atmospheric fluctuation and the thermal fluctuation of the detector systems is mostly common to the transmitted and reflected components. Therefore, these fluctuations are supposed to be removed by taking the difference of each signal. This technique is also applicable to MP-FT.

The PSI system analyzes the acquired data. Also, this unit performs mechanical control of MuFT. Baseline length vector source tracking and monitoring, mirror control, WG control and data acquisition are performed. Data analysis is also performed by the PSI system. Details of data analysis are explained in a forthcoming paper.

3.B. Detailed description of observables of MuFT

In this section, fundamentals of MuFT are fully described by treating electro-magnetic waves as vector waves. Suppose the electric field of the incident electromagnetic waves emitted from sky position $\boldsymbol{\theta}$ on the source plane at frequency ν described by $\vec{E}(\boldsymbol{\theta}, \nu, t) = (E_1, E_2)$ where E_1 and E_2 are orthogonal components of the electromagnetic waves. They can be written as,

$$\begin{aligned} E_1 &= \epsilon_1(\boldsymbol{\theta}, \nu) \cos(2\pi\nu t + \delta_1) = \epsilon_1(\boldsymbol{\theta}, \nu) \frac{\exp[2\pi j\nu t + j\delta_1] + \exp[-2\pi j\nu t - j\delta_1]}{2}, \\ E_2 &= \epsilon_2(\boldsymbol{\theta}, \nu) \cos(2\pi\nu t + \delta_2) = \epsilon_2(\boldsymbol{\theta}, \nu) \frac{\exp[2\pi j\nu t + j\delta_2] + \exp[-2\pi j\nu t - j\delta_2]}{2}. \end{aligned} \quad (11)$$

The phases for the fixed frequency, δ_1 and δ_2 , can be treated as time-independent variables. In option 1, WG1 and WG2 reflect the same polarization components of the incident electromagnetic waves. Therefore, option 1 measures the mutual coherence of the same component of the electromagnetic waves. In option 2, the components reflected by WG 1 and WG 2 are orthogonal to each other. Therefore, option 2 measures the mutual coherence of the orthogonal polarization components of the electromagnetic waves. For each option, there are two independent possible alignments of WGs, as explained in the previous subsection. The observed intensity transmitted through WG A for each option is expressed as

$$\begin{aligned} I_{Op1}(\mathbf{b}, x) &= \frac{1}{4} \int_{\Omega} \left(\int A_{\nu}(\boldsymbol{\theta}) \frac{\epsilon_1^2}{2} \left\{ 2 + \exp \left[-2\pi j\nu \left(\mathbf{b} \cdot \boldsymbol{\theta} - \frac{2x}{c} \right) \right] \right. \right. \\ &\quad \left. \left. + \exp \left[2\pi j\nu \left(\mathbf{b} \cdot \boldsymbol{\theta} - \frac{2x}{c} \right) \right] \right\} d\nu \right) d^2\theta, \\ I_{Op2}(\mathbf{b}, x) &= \frac{1}{2} \int_{\Omega} \left(\int \frac{A_{\nu}(\boldsymbol{\theta})}{2} \left\{ \epsilon_1\epsilon_1 + \epsilon_2\epsilon_2 \right. \right. \\ &\quad \left. \left. + \epsilon_1\epsilon_2 \exp[j(\delta_1 - \delta_2)] \exp \left[-2\pi j\nu \left(\mathbf{b} \cdot \boldsymbol{\theta} - \frac{2x}{c} \right) \right] \right. \right. \\ &\quad \left. \left. + \epsilon_1\epsilon_2 \exp[-j(\delta_1 - \delta_2)] \exp \left[2\pi j\nu \left(\mathbf{b} \cdot \boldsymbol{\theta} - \frac{2x}{c} \right) \right] \right\} d\nu \right) d^2\theta, \end{aligned} \quad (12)$$

where time averages were performed and $A_{\nu}(\boldsymbol{\theta})$ expresses a beam pattern of the observational system at frequency ν toward $\boldsymbol{\theta}$. The factors of 1/4 and 1/2 appearing in front of each integral come from the transmissivity and reflectivity at BS WG and output WG. Stokes Parameters are defined in the usual manner

$$\begin{aligned} \mathcal{I}(\boldsymbol{\theta}, \nu) &= [\epsilon_1(\boldsymbol{\theta}, \nu)\epsilon_1(\boldsymbol{\theta}, \nu) + \epsilon_2(\boldsymbol{\theta}, \nu)\epsilon_2(\boldsymbol{\theta}, \nu)], \\ \mathcal{Q}(\boldsymbol{\theta}, \nu) &= [\epsilon_1(\boldsymbol{\theta}, \nu)\epsilon_1(\boldsymbol{\theta}, \nu) - \epsilon_2(\boldsymbol{\theta}, \nu)\epsilon_2(\boldsymbol{\theta}, \nu)], \\ \mathcal{U}(\boldsymbol{\theta}, \nu) &= 2[\epsilon_1(\boldsymbol{\theta}, \nu)\epsilon_2(\boldsymbol{\theta}, \nu) \cos \delta], \\ \mathcal{V}(\boldsymbol{\theta}, \nu) &= 2[\epsilon_1(\boldsymbol{\theta}, \nu)\epsilon_2(\boldsymbol{\theta}, \nu) \sin \delta], \end{aligned} \quad (13)$$

where $\delta \equiv \delta_2 - \delta_1$ is the phase difference between the orthogonal components of the incident electromagnetic waves. By rewriting Eq.(12) in Stokes parameters, we have

$$I_{Op1} = \frac{1}{4} \int_{\Omega} \left\{ \int A_{\nu}(\boldsymbol{\theta}) \frac{\mathcal{I}(\boldsymbol{\theta}, \nu) \pm \mathcal{Q}(\boldsymbol{\theta}, \nu)}{2} \left[1 + \cos 2\pi \frac{\nu}{c} (\mathbf{b} \cdot \boldsymbol{\theta} - 2x) \right] d\nu \right\} d^2\theta,$$

$$I_{Op2} = \frac{1}{2} \int_{\Omega} \left\{ \int A_{\nu}(\boldsymbol{\theta}) \frac{1}{2} \left[\mathcal{I}(\boldsymbol{\theta}, \nu) + \left(\mathcal{U}(\boldsymbol{\theta}, \nu) \cos[2\pi \frac{\nu}{c}(\mathbf{b} \cdot \boldsymbol{\theta} - 2x)] \pm \mathcal{V}(\boldsymbol{\theta}, \nu) \sin[2\pi \frac{\nu}{c}(\mathbf{b} \cdot \boldsymbol{\theta} - 2x)] \right) \right] d\nu \right\} d^2\boldsymbol{\theta}, \quad (14)$$

where \pm corresponds to the alignment of the WGs, that is to CW or CCW alignments described in the previous subsection. These results show that the MuFT is capable of measuring all intensity distributions of 4 Stokes parameters in a wide band, eg. $\mathcal{I}(\boldsymbol{\theta}, \nu)$, $\mathcal{Q}(\boldsymbol{\theta}, \nu)$, $\mathcal{U}(\boldsymbol{\theta}, \nu)$ and $\mathcal{V}(\boldsymbol{\theta}, \nu)$. When the incident light is unpolarized, δ_1 and δ_2 are uncorrelated, and therefore, option 2 output is zero. For unpolarized sources, the intensity distribution can be measured by using option 1 (Ohta(2001)²¹, Hattori et al.(2000)²²). Details of experimental results of polarimetry with MuFT are presented in a forthcoming paper.

3.C. Spatial and spectral resolutions

Spectral resolution is determined by the maximum internal time lag, τ_0 , as $\Delta\nu \sim 1/\tau_0$. Spatial resolution for a fixed wavelength, λ , is defined in the same way as that of a conventional interferometer, and is limited by the maximum baseline length to λ/B_{max} . Since the wavelength coverage is very wide in the case of MuFT, the maximum spatial resolution is determined by the spatial resolution for minimum observable wavelength.

3.D. The field of view of the MuFT

Suppose broadband point-source observations with two apertures using MuFT. Define the center of the field of view (FOV) as the origin of the source coordinate. When the source position is $\vec{\theta}$, there is a geometrical time lag of $\tau_g = \mathbf{b} \cdot \boldsymbol{\theta}/c$. For simplicity, we assume that $\boldsymbol{\theta}$ is parallel to \mathbf{b} and $\mathbf{b} \cdot \boldsymbol{\theta} = b\theta$. As explained in Sec.2.B, the central burst of the interferogram for this source appears at $\tau = -\tau_g$. To detect the central burst for this source, τ_0 must be larger than τ_g . This condition provides a limit on the FOV of MuFT of $\theta < (c\tau_0)/b$. A similar constraint on the FOV is deduced in a different way. As discussed in the previous subsection, the finiteness of the maximum internal time lag leads to the spectral uncertainty of $\Delta\nu \sim 1/\tau_0$. The frequency uncertainty results in a phase uncertainty of $\delta\phi = 2\pi\Delta\nu b\theta/c$. To be able to observe a visibility function without significant coherent loss, $\delta\phi$ should be less than $\pi/2$. This condition provides almost the same limit on the FOV as shown in the above inequality. The limit shown above constrains the FOV only in the direction parallel to the baseline vector. In the direction perpendicular to the baseline vector, the above condition does not constrain the FOV. However, since the baseline vector must be rotated relative to the source plane for image synthesis, the same coverage of the FOV in both directions might be convenient. Therefore, the maximum available pixel number of the detector array installed on the focal plane of the MuFT is provided by $(c\tau_0/b\theta_p)^2$, where θ_p is the FOV of one detector pixel.

The analysis of the data measured by an off-axis pixel is not self-evident. Since the position of the central burst is shifted from the scanning center, the Fourier transformation of the obtained interferogram in τ from $-\tau_0$ to τ_0 causes a phase shift of $2\pi\nu\tau_g/c$. Therefore, the obtained phase

should be shifted back by $2\pi\nu\tau_g/c$. There are other non-trivial problems related to using the multi-pixel detector array on MuFT which must be studied to optimize methods. Rinehart et al. (2004)¹⁰ have been studying the application of the multi-pixel detector array on the double Fourier in laboratory experiments in optical wave bands using an optical CCD camera. They have successfully detected interferograms in each pixel which are each observing different FOV.

3.E. Phase errors, efficiencies and noise

There are four sources of phase errors: (1) sampling error due to shift in zero optical path difference; (2) uncertainty of (u, v) points due to finiteness of spectral resolution; (3) uncertainty of (u, v) points due to pointing error. (4) Atmospheric phase fluctuation. The first one can be compensated by zero-path calibration of the interferometer. The second one provides a limit on the FOV, as discussed in the previous subsection. The third one can be corrected by pointing observations of compact sources with a certain interval. Atmospheric phase error can be corrected when atmospheric opacity and phase error are correlated.

As seen in Eq.(12) and Eq.(14), optical efficiency of MuFT for a single output port is 1/8 for option 1 when unpolarized radiation is observed, combination of two output ports, such as that used for detecting reflection and transmission of WG A, would give an efficiency of 1/4. Detecting a signal traveling toward WG B would give an efficiency of 1/2. Furthermore, setting another MuFT under the first one to detect the radiation transmitted through WGs 1 and 2 would give an efficiency of 1.

Sources of noise in observed interferograms are atmospheric radiation, radiation from optical components, internal detector noise and other excess noise such as readout electronics noise. Since most of these noises are incoherent, they do not create coherent peaks in an interferogram but appear as random noise. Common amplitude fluctuation of atmospheric emission could be removed by taking the difference of the interferograms obtained by signals transmitted through and reflected by output WG. Radiation from optical components causes a small amount of coherent noise signal in an interferogram. Most of the noise emission from the optical components which propagate back to the input wire grids is ejected to the sky. However, the direction of noise emission propagated from optical components has a finite distribution, and finite errors in alignment of wire grids and optical components are not escapable. Therefore, a small amount of radiation returns to the detector. This results in an autocorrelation noise emission signal from the optical components in the interferogram. This can be removed by subtracting the background interferogram obtained by observations of the sky without source. However, it is impossible to observe exactly the same sky as during source observations without the source. We have to adopt data obtained by observations of the sky without the source as the background data.

4. Advantages of MuFT

One of the most prominent advantage of MuFT is that one can use direct detectors like a bolometer as an interferometer focal plane detector. This give MuFT the following three significant advantages.

High sensitivity and wide bandwidth interferometer in FIR As described in the introduction, the sensitivity of direct detectors is higher than that of heterodyne receivers in the frequency range of $\nu > 100$ GHz, that is $\lambda < 3$ mm. Therefore, the sensitivity of MuFT could be higher than an interferometer based on heterodyne receivers, especially in submillimeter and FIR wave bands. Performing wide band observations with direct detectors is easily achieved. For example, bolometers which have a sensitivity in extremely broadband have been used as focal plane detectors of FTS in FIR wave bands. Since the WGs have uniform reflectivity and transmissivity for all frequencies in millimeter, submillimeter and FIR, the MuFT is suited to broadband observations.

Wide field of view Constructing large format heterodyne focal plane arrays is not yet feasible, since local oscillators and associated electrical circuits for each detector are bulky and not amenable to automated production using integrated circuit technology. Therefore, not a single detector is used in radio interferometers, including ALMA. This severely limits the FOV of the interferometer. On the other hand, large format focal plane arrays of direct detectors are already operating. New types of direct detectors aiming at a dramatic increase in the number of pixels are lying developed.^{5,6} Since MuFT can use direct detectors as interferometer focal plane detectors, it could extend the FOV of the millimeter and submillimeter interferometers dramatically. Details are described in Sec.3.D.

Large dynamic range When source intensity distribution is independent of frequency, we can sum up all images obtained at different frequencies into a single image, as described in Sec.2.A. In other words, a single baseline observation is equivalent to observations with many combinations of baseline interval in the case of a single frequency interferometer. Long wavelengths observe overall source structures with low spatial resolution. Short wavelengths observe fine structures with high spatial resolution. A large dynamic range of spatial resolution is covered even by a single baseline observation. A similar technique has been addressed as MFS for heterodyne interferometer(Conway et al.(1990)¹⁴). This is a technique for combining maps obtained for different frequencies by different interferometers into a single image.

Linear and Circular Polarimetry The MuFT can measure all 4 components of Stokes parameters (Hattori et al.(2000)²²), as explained in sec. 3.B. This is because MuFT uses WGs as beam-splitter. Since a double Fourier uses dielectric film as a beam-splitter, it cannot perform polarimetry.

5. Summary

We proposed a new type of bolometric interferometer named MuFT by applying MP-FT to aperture synthesis. Fundamentals of imaging, spectroscopy and polarimetry with this instrument were developed. The MuFT is a system which permits imaging and spectroscopy in a wide band by combining the Wiener-Khinchine Formula¹³ which makes it possible to extract a spectrum from the auto-correlation and van Cittert Zernike Formula¹³ which allows imaging from the mutual

correlation. The concrete composition of this equipment was proposed. By combining wire grid beam-splitters adequately, source intensity distributions of four Stokes parameters can be acquired in a wide band. Fundamental restrictions in practical use were discussed.

We are planning to perform the observations from good mm and submillimeter observation sites, such as the Nobeyama Radio Observatory in Japan, the Atacama desert in Chile, South Pole etc.. The possibility of having a super-wide FOV by mounting the focal plane array of bolometers, SIS photon detectors and transition edge sensors is attractive for future applications. Optical designs of MuFT for using detector arrays is going to be advanced.

Applying this technique to a space-borne mission is one of the best possibilities for extracting the maximum ability of MuFT, since there is no restriction on the bandwidth from atmospheric absorptions. Mather et al.²³ has been proposing a space-borne FIR observatory based on this kind of technique. The future application of this technique to observations from space could open new and interesting possibilities in FIR astronomy.

ACKNOWLEDGMENTS

The research was financially supported by the COE program "Exploring New Science by Bridging Particle-Matter Hierarchy" at Tohoku University, the Sasagawa Scientific Research Grant and the Japan Science Society and by the Grant-in-Aid for Scientific Research (116204010) of the Japan Society for the Promotion of Science. We would like to thank Ms. Y. Luo of Tohoku university and Ms. Y. McLean of arkitext.com for critical reading of English. At last, thanks are due to Dr. J. Nishikawa of NAOJ for helpful suggestions and comment about established optical and IR interferometers system.

References

1. A. R. Thompson, J. M. Moran and G. W. Swenson, Jr., *Interferometry and Synthesis in Radio Astronomy*, 2nd edition, (Wiley-Interscience, 2001).
2. M. Ishiguro, K.-I. Morita, T. Kasuga, T. Kansawa and H. Iwashita "The Nobeyama millimeter-wave interferometer," in *Proceedings of International symposium on Millimeter and Submillimeter Wave astronomy (A86-41201 19-88)*, (Granada, Spain, September 11-14, 1984), pp. 75–84, 1985.
3. T. L. Wilson, A. J. Beasley and H. A. Wootten "Status of the Atacama Large Millimeter Array," presented at the Cool Universe: Observing Cosmic Beginnings 2004, Chile, 4–8 Oct. 2004.
4. J. Rieke, *Detection of light*, 2nd edition, (Cambridge University press, 2003).
5. D. J. Benford, S. R. Dicker, E. J. Wollack, M. P. Supanich, J. G. Staguhn, S. H. Moseley, K. D. Irwin, M. J. Devlin, J. A. Chervenak, and T. C. Chen "A planar two-dimensional superconducting bolometer array for the Green Bank Telescope," in *Millimeter and Submillimeter Detectors for Astronomy II*, J. Zmuidzinas, W. S. Holland, and S. Withington, eds., *Proceedings of the SPIE* **5498**, 208-219 (2004).

6. H. Matsuo, S. Ariyoshi, C. Otani, H. Ezawa, J. Kobayashi, Y. Mori, H. Nagata, H. M. Shimizu, M. Fujiwara, M. Akiba, and I. Hosako “Design of wide-field submillimeter-wave camera using SIS photon detectors,” in *Millimeter and Submillimeter Detectors for Astronomy II*, J. Zmuidzinas, W. S. Holland, and S. Withington, eds., Proceedings of the SPIE **5498**, 371-380, (2004)
7. J. Zmuidzinas, “The Role of Coherent Detection,” in *New Concepts for Far-Infrared and Submillimeter Space Astronomy* (D. Benford and D. T. Leisawitz, eds.), NASA CP-2003-212233, pp. 329-341, Washington, DC: NASA, 2003.
8. K. Itoh and Y. Ohtsuka, “Fourier-transform spectral imaging - Retrieval of source information from three-dimensional spatial coherence,” *Optical Society of America Journal* **3** 94-100 (1986).
9. J.-M. Mariotti and S. T. Ridgway, “Double Fourier spatio-spectral interferometry - Combining high spectral and high spatial resolution in the near infrared,” *Astronomy and Astrophysics* **195** 350-363 (1988).
10. S. A. Rinehart, T. Armstrong, B. J. Frey, J. Kirk, D. T. Leisawitz, D. B. Leviton, L. Lob-singer, R. Lyon, A. J. Martino, T. Pauls, L. G. Mundy, and E. Sears “The Wide-Field Imaging Interferometry Testbed I: Progress, Results, and Future Plans,” in *New Frontiers in Stellar Interferometry*, W. A. Traub, eds., Proceedings of SPIE **5491**, 920-931 (2004).
11. D. H. Martin and E. Puplett, “Polarized Interferometric Spectrometry for the Millimetre and Submillimetre Spectrum,” *Infrared Physics*, **10**, 105-109 (1969).
12. I. S. Ohta, *Development of Astronomical Interferometer applying Fourier transform spectroscopy to aperture synthesis system in mm and sub-mm band*. PhD thesis, Tohoku University, 2004.
13. M. Born and E. Wolf, *Principle of Optics 5th edition*, (PERGAMON PRESS LTD.(Oxford, U.K.), 1975), Chap. 10.
14. J.E.Conway, T.J.Cornwell and P.N.Wilkinson, ”Multi-frequency synthesis: a new technique in radio interferometric imaging,” *Mon.Not.R.astr.Soc.* **246**, pp.490-509, 1990
15. R. A. Sunyaev and B. Ya. Zel’dovich, ”The observations of relic radiation as a test of the nature of X-ray radiation from the clusters of galaxies,” *Comments on Astrophysics and Space Physics* **4**, pp. 173-178, 1972
16. M. Hattori and N. Okabe, ”A direct method for measuring heat conductivity in intracluster medium,” *The Astrophysical Journal***625**, pp.741-747, 2005
17. M. Shao, M. M. Colavita, B. E. Hines, D. H. Hutter, K. J. Johnston, D. Mozurkewich, R. S. Simon, J. L. Hershey, J. A. Hughes, and G. H. Kaplan, ”The Mark III stellar interferometer,” *Astronomy & Astrophysics* **193**, pp. 357-371, 1988
18. B. S. Mason, T. J. Pearson, A. C. S. Readhead, M. Shepherd, J. Sievers, P. Udomprasert, J. K. Cartwright, and S. Padin, ”First results from the CBI”, *AIP Conference Proceedings* **586**, pp. 178-183, 2001
19. K. Y. Lo, T. H. Chiueh, R. N. Martin, Kin-Wang Ng, H. Liang, Ue-li Pen, Chung-Pei Ma, M. Kesteven, R. Sault, R. Subrahmanyan, W. Wilson, and J. Peterson, ”AMiBA: Array for microwave background anisotropy,” *AIP Conference Proceedings* **586**, pp. 172-177, 2001

20. J. C. Mather and D. Leisawitz, “The SPIRIT and SPECS Far-Infrared/Submillimeter Interferometry Missions,” *The Institute of Space and Astronautical Science Report SP No. 14*, p. 219-224. **14**, pp. 219–224, Dec. 2000.
21. I. S. Ohta, *Application of Aperture Synthesis type Interferometer with Martin and Puplett type Fourier transform spectrometer*. Master thesis, Tohoku University, 2001.
22. M. Hattori, I. S. Ohta, H. Matsuo, and Y. Shibata, “The Application of MP-FTS to Aperture Synthesis,” *The Institute of Space and Astronautical Science Report SP 14*, pp. 353–360, Dec. 2000.
23. J. C. Mather, S. H. Moseley, Jr., D. Leisawitz, E. Dwek, P. Hacking, M. Harwit, L. G. Mundy, R. F. Mushotzky, D. Neufeld, D. Spergel, and E. L. Wright, “The Submillimeter Frontier: A Space Science Imperative,” *ArXiv Astrophysics e-prints* , Dec. 1998.

List of Figure Captions

Fig. 1. Coordinate systems and designations used in observation of extended source. Source is assumed to be very far away.

Fig. 2. Simplified schematic diagram of MuFT. Wave-front division of source light is performed by LiC. These are combined by FI, through optical systems. Interferogram is measured by DeS.

Fig. 3. Example of FI unit. WG position is Option1. Thin dashed lines show light paths. Arrows attached to the dashed lines indicate the propagation direction of the light beams.

Fig. 4. Two basic configurations of wire grids 1 and 2. The left figure is Option.1 (WGs are parallel) and the right figure is Option.2 (WGs are perpendicular). Gray lines are light paths.

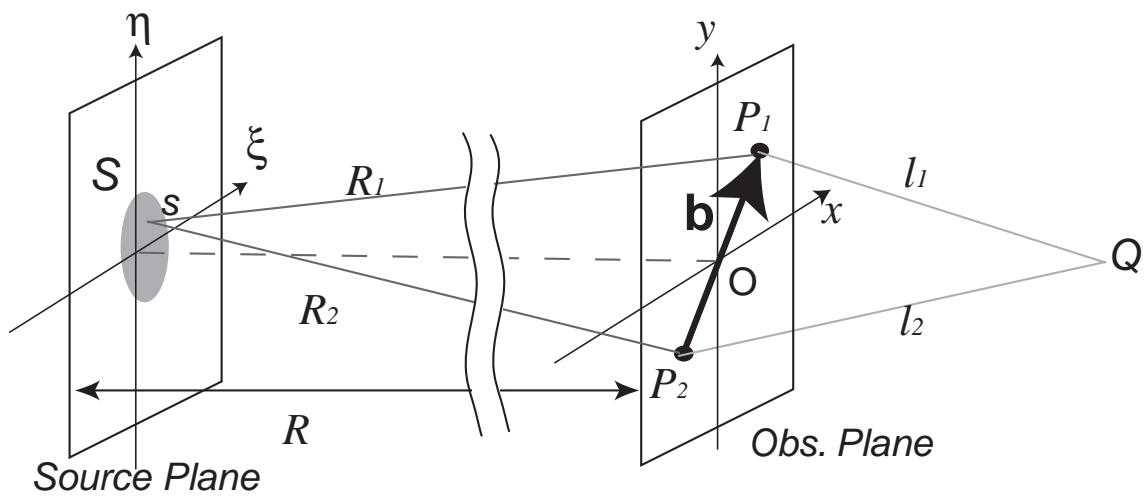


Fig. 1. Coordinate systems and designations used in observation of extended source. Source is assumed to be very far away.

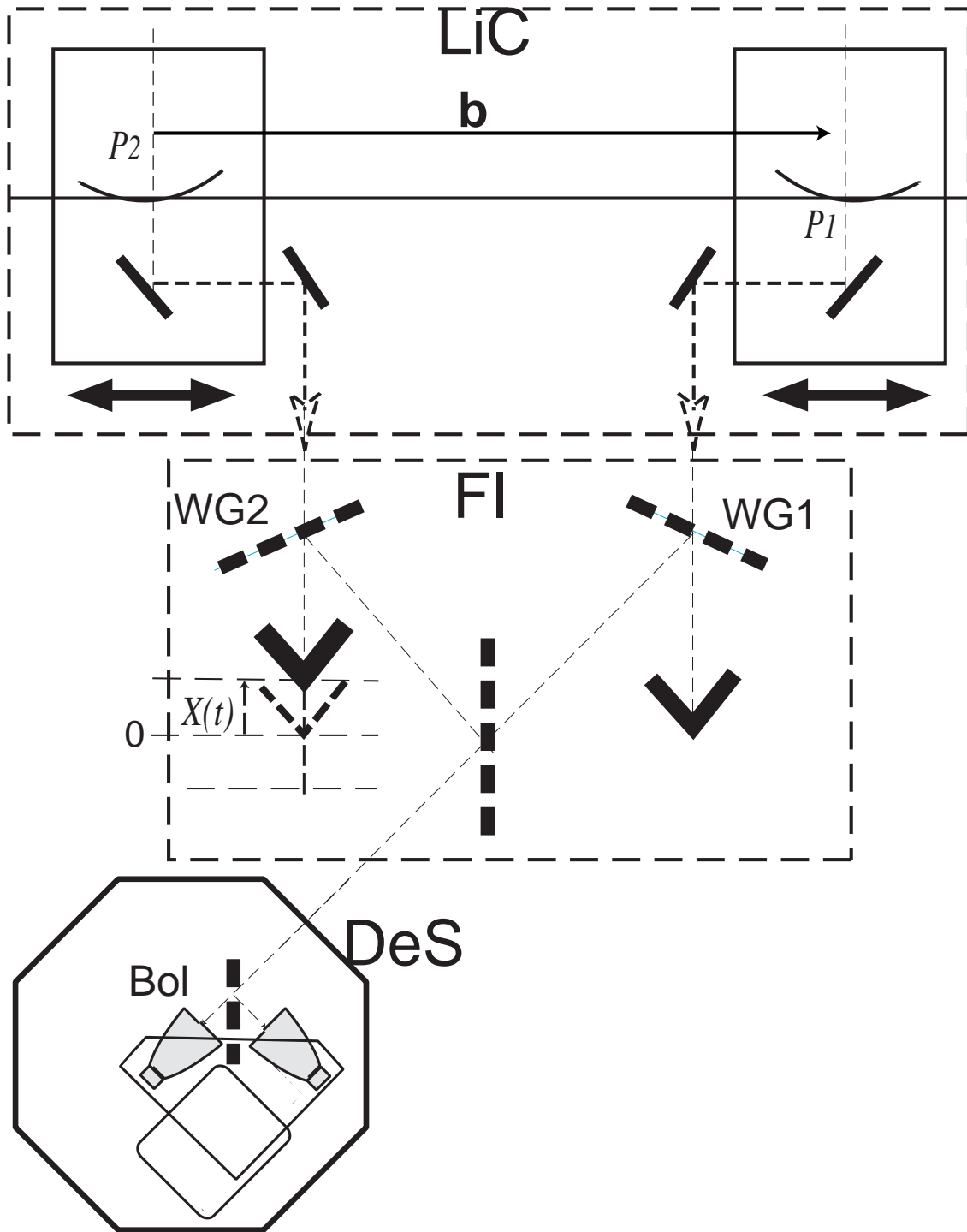


Fig. 2. Simplified schematic diagram of MuFT. Wave-front division of source light is performed by LiC. These are combined by FI, through optical systems. Interferogram is measured by DeS.

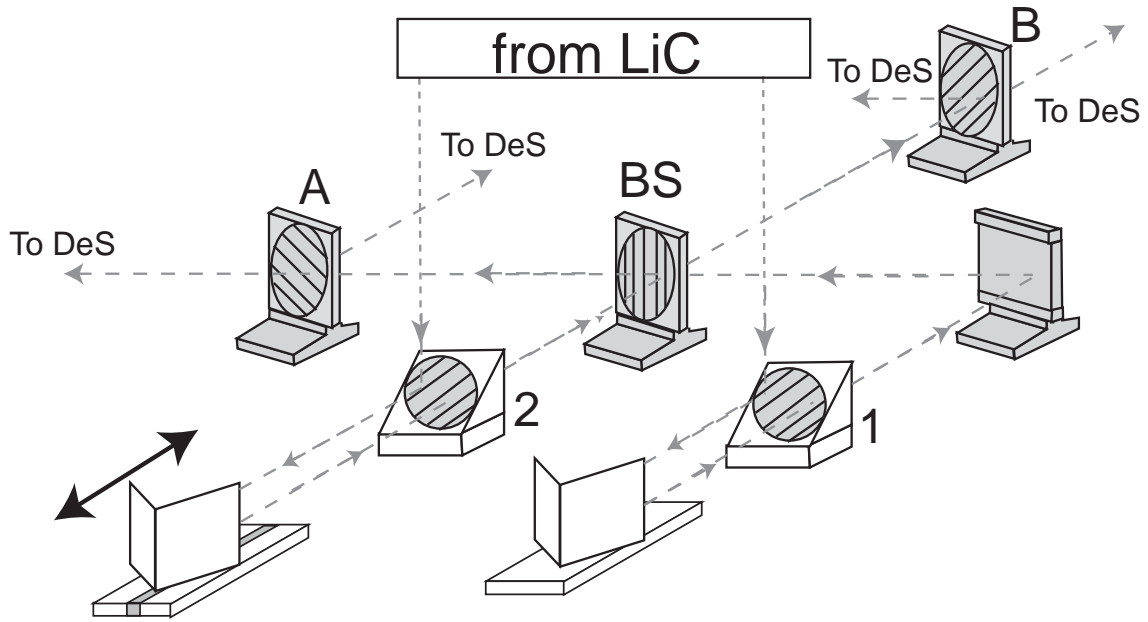


Fig. 3. Example of FI unit. WG position is Option1. Thin dashed lines show light paths. Arrows attached to the dashed lines indicate the propagation direction of the light beams.

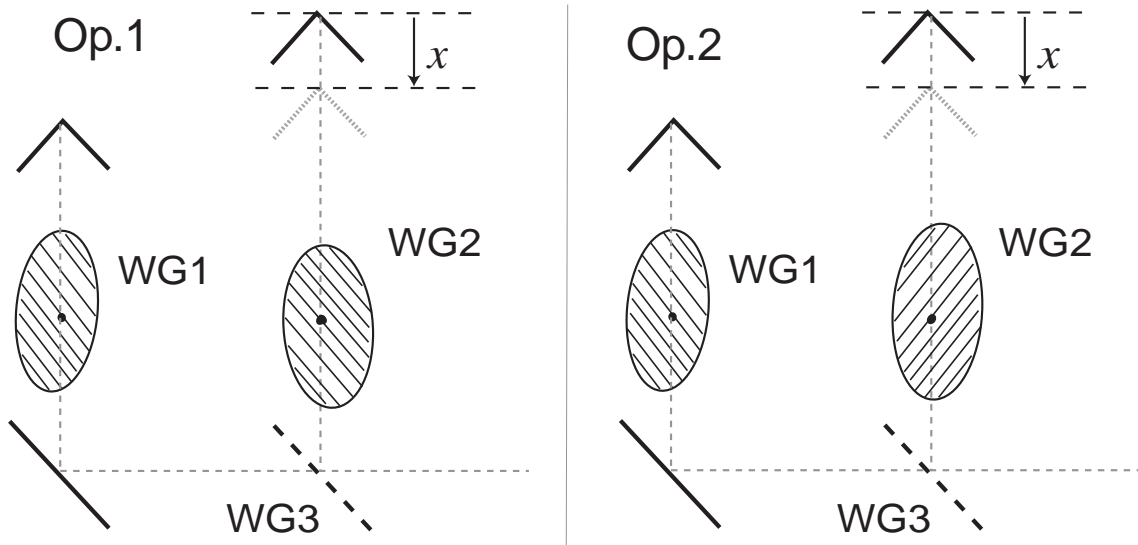


Fig. 4. Two basic configurations of wire grids 1 and 2. The left figure is Option.1 (WGs are parallel) and the right figure is Option.2 (WGs are perpendicular). Gray lines are light paths.